



Microstructural and Tribological Characteristics of Sn-Sb-Cu-Based Composite Coatings Deposited by Cold Spraying

W. Tillmann¹ · L. Hagen¹ · M. D. Kensy¹ · M. Abdulgader¹ · M. Paulus²

Submitted: 6 December 2019 / in revised form: 27 April 2020
© The Author(s) 2020, corrected publication 2021

Abstract Sn-based Babbitt coatings are widely used for sliding in hydrodynamic bearings. The Babbitting of bearing surfaces is among others accomplished by casting; however, this implies some disadvantages such as segregations, or susceptibility to shrinkage defects. Thermal spraying represents a promising method to overcome these challenges. To date, no studies on Babbitt coatings deposited by means of low-pressure cold spraying (LPCS) are available in the literature. In this study, a first attempt is made to produce a Sn-Sb-Cu-based composite coating reinforced with alumina particles by means of LPCS which enables the coating of internal diameters (IDs) of cylindrical components. A tailor-made feedstock was utilized which consists of a powder mixture of Sn, Sb, Cu and alumina. The composite coating is investigated with regard to its microstructural and tribological characteristics using scanning electron microscopy (SEM), energy-dispersive x-ray spectroscopy (EDS), x-ray diffraction (XRD), as well as dry sliding experiments. Metallographic investigations demonstrate the feasibility of depositing an alumina-reinforced Sn-Sb-Cu-based composite coating with a dense microstructure and low porosity. The composite coating mainly consists of Sn, SbSn, Cu and hexagonal Cu₃Sn. Despite a small fraction of alumina particles, the microhardness of the composite coating is primarily determined by the formation of SbSn intermetallic phases dispersed in the soft Sn-Sb-rich matrix. The composite coating

possesses a coefficient of friction of 0.43 ± 0.01 and wear coefficient k of $17.27 \pm 7.77 \times 10^{-5} \text{ mm}^3 \text{ N m}^{-1}$ sliding against a 100Cr6 counterbody.

Keywords Babbitt · bearings · low-pressure cold spraying · tribology

Introduction

Babbitt, also called white metal, represents a group of alloys that contain different grades based on Sn or Pb, with the addition of Cu and Sb. Despite their higher cost, Sn-based Babbitt alloys are widely used in preference to Pb-based Babbitt alloys due to their excellent corrosion resistance, and less tendency toward segregation. The addition of Cu and Sb, inter alia, determines the strength of the materials. The microstructure of Sn-Sb-Cu-based Babbitt alloys mainly consists of a soft solid solution matrix interstratified with intermetallic phases such as SbSn and Cu₆Sn₅. Cu atoms tend to interact much more strongly with Sn than with Sb to form Cu₆Sn₅ as compared with SbSn (Ref 1, 2). The formation of Cu₆Sn₅ or Cu₃Sn in part results from the interaction of Cu with liquid Sn. Cu₃Sn usually arises from the formation of Cu₆Sn₅ (Ref 3, 4), wherein the formation of Cu₃Sn necessitates an increased Cu content and higher temperatures. With regard to the Cu-Sn phase equilibrium, Yin et al. (Ref 3) also stated the possible formation of a Cu₄₁Sn₁₁ phase, which is thermodynamically stable and originates from Cu₃Sn at low temperatures. Nonetheless, for common Cu contents, the formation of Cu₃Sn and Cu₄₁Sn₁₁ is more unlikely. Cu₆Sn₅ reveals a predominant compound with an allotropic transformation at 186 °C, from a monoclinic crystal structure at lower temperatures to a hexagonal crystal

✉ L. Hagen
leif.hagen@udo.edu

¹ Institute of Materials Engineering, TU Dortmund University, Dortmund, Germany

² Fakultät Physik/DELTA, TU Dortmund University, Dortmund, Germany

structure at higher temperatures (Ref 5, 6). The hexagonal phase can be stabilized with the addition of further elements (Ref 7, 8). Thus, the inclusion of small amounts of Sb in $\text{Cu}_6\text{Sn}_{5-x}\text{Sb}_x$ shifts the region of thermal stability from 186 °C down to room temperature (Ref 8). Nevertheless, it was found that high concentrations of Sb cause multiple agglutinations of SbSn crystals in the matrix (Ref 9), while high concentrations of Cu favor the emergence of Cu-Sn intermetallic compounds, which leads to a reduced toughness simultaneously (Ref 10).

Studies showed that further alloying elements can be used to obtain a microstructure refinement, i.e., Sb-Sn and Cu-Sn intermetallic precipitates. Together with solid solution hardening effects, the refinement can lead to improved mechanical properties (Ref 11). An increase in strength can also be achieved by dispersive hardening with micron-sized particles such as the introduction of high-modulus reinforcing particles into the metallic matrix, i.e., of Babbitt. Kalashnikov et al. (Ref 12) investigated the tribological characteristics of surfacing rods and coatings based on B83 Babbitt (B82 is a grade specification for various Sn-based and Pb-based white metal bearing alloys established by the American Society for Testing and Materials) (Ref 13) reinforced with different ceramic particles. As obtained from dry sliding tests, the introduction of high-strength micron-sized ceramic particles improves the tribological behavior. Compared to the conventional Babbitt coating, the Babbitt composite coating reinforced with ceramic particles exhibits several positive effects: (1) a reduced coefficient of friction (COF); (2) a more constant COF throughout the load interval; (3) a reduced wear rate. The latter was also confirmed in (Ref 14) for an alumina-reinforced Babbitt coating.

Babbitt coatings are widely used in plain and journal bearings. The soft solid solution matrix acts as solid lubricant and allows the embedding of abrasive particles, whereas the intermetallic phases dispersed in the matrix lead to an adequate hardness, thus enabling a sufficient load carrying capacity (Ref 15). With regard to industrial bearings, Babbitt coatings mainly serve as sacrificial surface (Ref 16). As a result of an unwanted contact between sliding surfaces, the softer Babbitt surface wears out to protect the counterpart from significant damage (Ref 17), or to permit deformation to accommodate some misalignment of the bearing surfaces (Ref 18). Moreover, Babbitt coatings exhibit good emergency running properties in the absence of adequate lubrication, since Sn provides the ability to melt at low temperature and to act as liquid lubricant (Ref 17, 19).

Babbitting of bearing surfaces can be accomplished by casting, welding, as well as thermal spraying (Ref 12). Babbitting by means of casting implies some disadvantages: low adhesive strength of the coating to the substrate,

tendency toward segregation, susceptibility to shrinkage defects, as well as the necessity to keep a high allowance for machining. Despite ameliorated manufacturing capacities (i.e., casting process control, or new casting processes), not all technical problems were solved to date by new casting processes. In contrast, thermal spraying represents a promising method to overcome these challenges. Thus, thermal spraying enables the ability of depositing near-net-shape coatings coupled with good adhesion to the substrate. Due to the inherent process characteristics (i.e., the thermo-kinetics by depositing molten, semi-molten or solid spray particles), segregations and shrinkage defects are nearly precluded. Among thermal spraying, several studies already revealed the feasibility of the deposition of Babbitt coatings using flame spraying (Ref 19-21), plasma spraying (Ref 21, 22), high-velocity oxy-fuel spraying (Ref 17) and arc spraying (Ref 9, 20). Furthermore, a patent by Lamberton et al. (Ref 23) disclosed a cold spray coating process for depositing Babbitt coatings on the inner surfaces of a bearing assembly. However, no studies on the microstructure are presented by the authors. Junior et al. (Ref 20) recently investigated the microstructural and tribological characteristics of Babbitt coatings (ASTM B23 grade 2) deposited by arc spraying and flame spraying and compared the findings with those obtained from coatings deposited by centrifugal and conventional casting processes. The authors clarified that the thermally sprayed Babbitt coatings exhibit, despite a higher porosity, an enhanced wear resistance in dry sliding experiments compared to the conventional Babbitt surfaces. The authors stated that the superior wear resistance is attributed to the fact that the precipitates formed in the thermally sprayed Babbitt coatings are more refined than those observed in deposits produced by common processes.

Although Sn-Sb-Cu-based feedstocks are widely available, to date no studies on Babbitt coatings deposited by means of LPCS are available in the literature. The absence of such studies currently does not allow a comparison between the coating properties of conventional Babbitt coatings and low-pressure cold gas-sprayed Babbitt coatings. Among thermal spraying, LPCS represents a cost-saving method without the usage of fuel gases or liquid fuels, with the ability to recondition or repair coatings of worn surfaces, even on site, directly on the customer's premises as the spray equipment is transportable. In LPCS, the temperature of the process gas is below the melting point of the feedstock; accordingly, particles are not melted in the gas flow. Studies verified preheating temperatures of the propellant gas (nitrogen or air) up to 650 °C (Ref 24, 25) or rather 700 °C (Ref 26), with the working range for low-melting materials usually being in the range of 440-540 °C (Ref 25), or 300-500 °C (Ref 24), respectively. Due to the inherent process characteristics, in most cases a

certain amount of high melting hard particles such as alumina is added to the feedstock (Ref 27, 28). According to Koivuluoto et al. (Ref 27), the admixture of alumina has three functions: (1) to prevent nozzle-clogging; (2) to activate the sublayer surface by the removal of foreign substances, impurities and oxide layers as well as surface roughening; (3) to strengthen the coating microstructure due to the insertion of hard particles (Ref 29). Winnicki et al. (Ref 26) also demonstrated that within the addition of alumina particles to metal powder the adhesion of low-pressure cold-sprayed coatings could be greatly improved due to the fact the impinging alumina particles lead to a densification of the microstructure.

The growing market for industrial applications such as bearings requires in part the coating of IDs. Despite individual studies on the coating of internal bore features by means of cold spraying (Ref 30, 31) using modified nozzle configurations, no studies exist so far dealing with the ID coating through the use of LPCS. In this study, a first attempt is made to produce a Sn-Sb-Cu-based composite coating reinforced with micron-sized alumina particles by means of LPCS. An adaptation of the nozzle configuration is presented, which enables the coating of IDs of cylindrical components. The produced coating is investigated with regard to its microstructural and tribological characteristics. The findings are compared and discussed with those reported for Sn-Sb-Cu-based coatings, i.e., Babbitt coatings, deposited by arc and flame spraying as well as conventional manufacturing techniques such as casting.

Experimental Setup

Substrate Material and Feedstock

C45 steel (1.0503) round flat specimens with a diameter of 40 mm and a thickness of 6 mm were used as substrate. Prior to the coating deposition, the substrates were grit blasted with corundum (grit size: $-150 + 106 \mu\text{m}$) using a blasting air pressure of 0.4 MPa, a stand-off distance of 100 mm and a blasting angle of approximately 45° . Afterward, the specimens were soaked in an ultrasonic ethanol bath to remove oil and corundum residues.

A tailor-made feedstock was manufactured in-house according to the specification ASTM B23 grade 3. The powder mixture consists of 84.0 wt.% of Sn, 8.0 wt.% of Sb and 8.0 wt.% of Cu. Additionally, the feedstock was mixed with alumina using a volumetric ratio of 80:20 to minimize the risk of nozzle-clogging during spraying. Table 1 shows the volumetric particle size distribution with its 10th (D10), 50th (D50) and 90th percentile (D90) for each constituent measured by laser light scattering (particle analyzer S3500, Fa. Microtrac, Germany). Before applying

Table 1 Volumetric particle size distribution determined by laser light scattering

Elements	D10, μm	D50, μm	D90, μm
Sn	6.74	17.98	47.45
Sb	3.90	16.66	35.64
Cu	13.62	29.69	50.28
Al ₂ O ₃	11.49	18.11	28.99

the feedstock to the powder feeder system, it was homogenized with a TURBULA T2F mixer (Fa. Willy A. Bachofen, Switzerland) for 3 h.

Scanning electron microscope (SEM) imaging and the corresponding EDS maps obtained from O K α , Al K α , Cu K α , Sn L α and Sb L α depict the different constituents of the powder mixture after homogenization (Fig. 1). The brightness in the BSE imaging illustrates the different chemical composition. Many Sn-Sb-rich particles (bright phases) exhibit a spherical shape (or irregular shape in the case of Sb particles), whereas the Cu particles (light gray phase) show a dendritic-like structure. As opposed to that, the fused and crushed alumina particles (dark gray phase) are characterized by an angular blocky shape.

Coating Deposition

In order to conduct the spraying experiments, a portable DYMET 413 spraying system (Fa. Dycomet, Netherlands) was utilized. The spray gun was equipped with an in-house-made extension and nozzle attachment to enable the ID coating (Fig. 2). The conventional nozzle configuration was further modified based on the results obtained from preliminary tests to minimize the risk of nozzle-clogging, while reducing the spraying distance to a minimum. Due to the technical changes, it is possible to coat cylindrical components with an ID of 140 mm.

The spray gun was mounted on a three-axis CNC linear drive (Fa. Antriebstechnik Carl Rehfuß Albstadt, Germany). The spray parameters used within this study are listed in Table 2. The spraying experiments were conducted using oil-free compressed air. The temperature of the propellant gas was set to nearly 400°C and was evaluated by using thermocouples at the injection point of the feedstock prior to the coating deposition. With the use of a collecting container, a powder feed rate of approximately 112 g/min was determined gravimetrically.

Analytic Methods

Prior to the metallographic investigations, cross sections of coated samples were prepared using silicon carbide

Fig. 1 SEM image and EDS maps obtained from O K α , Al K α , Cu K α , Sn L α and Sb L α showing the element concentrations of the components of the powder mixture

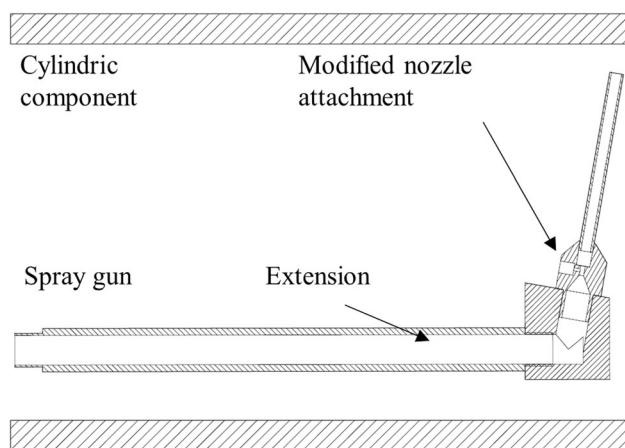
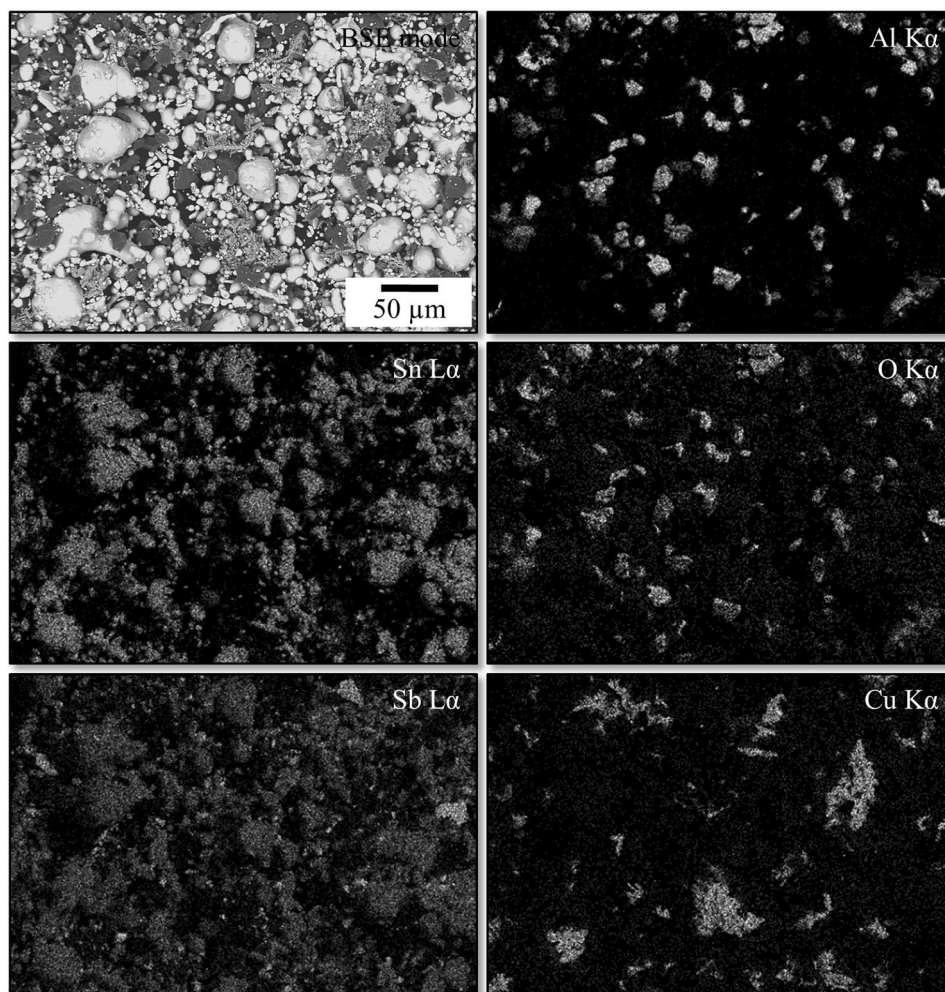


Fig. 2 Schematic drawing of the custom-made extension and nozzle attachment

grinding disks and polishing cloths with diamond suspension (abrasive particle size: 6, 3 and 1 μm). The microstructural characteristics were examined by means of electron microscopy and energy-dispersive x-ray

Table 2 Spray parameter settings

Spray parameters	Value
Gas temperature, $^{\circ}\text{C}$	~ 400
Gas pressure, bar	5.0
Stand-off distance, mm	10
Spray angle, $^{\circ}$	100
Transverse speed, mm/s	100
Powder feed rate, g/min	112
Overruns, passes	4

spectroscopy (EDS) through a field emission scanning electron microscope (FE-SEM) (type JSM-7001F, Jeol, Germany) equipped with secondary electrons (SE), backscattered electrons (BSE) as well as energy-dispersive x-ray detectors (Oxford Instruments, United Kingdom). The data were analyzed with the EDS microanalysis software INCA (Oxford Instruments, United Kingdom). The porosity was determined via x-ray microcomputed

tomography (Xradia 520 Versa, Zeiss, Germany) from a free-standing sampling (geometry of sampling: $2000\ \mu\text{m} \times 2000\ \mu\text{m} \times 200\ \mu\text{m}$). The alumina content, i.e., the content of alumina particles distributed in the coating, was determined by grayscale analysis of cross-sectional images taken at $200 \times$ magnification of the cross section at five different spots. The phase composition was investigated by means of x-ray diffraction (XRD) at the beamlines BL9 and BL2 of the synchrotron light source DELTA (Dortmund, Germany). The photon energy was set to 13 keV (BL9, wavelength $\lambda = 0.9536\ \text{\AA}$) and 12.32 keV (BL2, $\lambda = 1.001\ \text{\AA}$). A PILATUS 100 k detector (DECTRIS, Switzerland) at the BL9 and MAR345 image plate detector (marXperts, Germany) at the BL2 were used for photon detection. The beam size was set to $1.0 \times 0.1\ \text{mm}^2$ (BL9) and $1 \times 1\ \text{mm}^2$ (BL2), and the angle of the incidence was 5° . The software MATCH! in conjunction with a reference database (i.e., Crystallography Open Database) was used to identify the phase composition. The tribological characteristics of the manufactured Babbitt coating were evaluated in dry sliding experiments. Prior to the tribological test, the coating surface was machined using silicon carbide grinding disks and polishing cloths with a diamond suspension (abrasive particle size: 6, 3 and $1\ \mu\text{m}$). The tribological tests were performed using a ball-on-disk tribometer (CSM Instruments, Switzerland). The sliding tests were carried out at room temperature without lubricant supply against a 100Cr6 counterbody (ball with 6 mm in diameter, and a hardness of $11.31 \pm 0.13\ \text{GPa}$). The sliding velocity was kept constant at 0.4 m/s. A load of 5 N was applied, while 10,000 revolutions were conducted on constant radius which corresponds to a sliding distance of approximately 950 m. The coefficient of friction (COF) was determined via measurements of the tangential force and the applied normal force. In order to calculate the wear coefficient of both the Sn-Sb-Cu-based coating (k) and the 100Cr6 counterbody (k_{ball}), the volumetric material loss of each tribo-partner was measured by 3D-profilometry (device Infinite Focus, Fa. Alicona, Austria). With regard to the tribological stressed coating surface, the volumetric material loss was captured at four different positions at the wear track taking three samples into account. The wear tracks were further investigated by means of electron microscopy and EDS using a FE-SEM as described previously. To identify strain hardening effects at the tribological stressed coating surface, Vickers microhardness measurements were carried out inside the wear track as well as at the non-tribological stressed surface section of the coating using a Duramin-40 microhardness tester (Struers, Germany) with a load of 2.49 N (300gf). A minimum of five indents were conducted for the microhardness measurement.

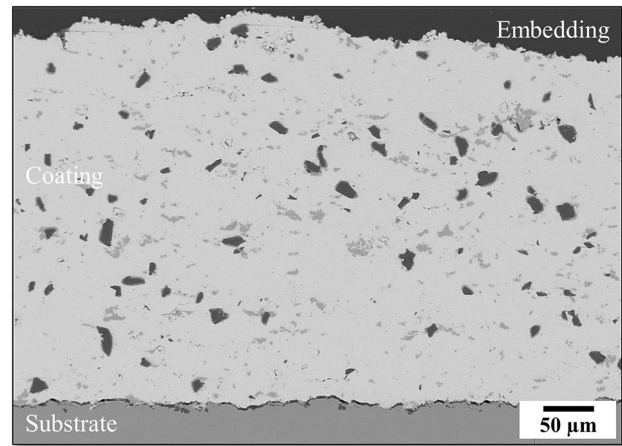


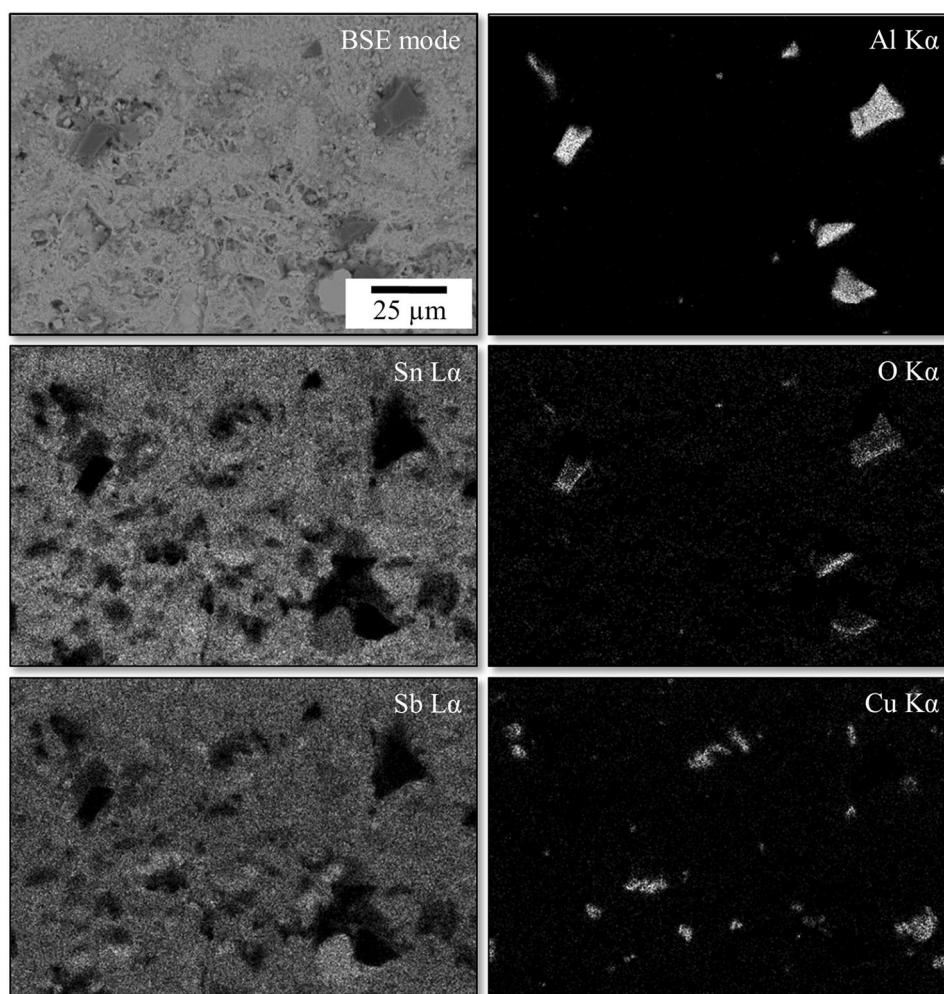
Fig. 3 Cross section of the coating microstructure

Results and Discussion

Microstructural Characteristics

Figure 3 illustrates the microstructure of the low-pressure cold-sprayed alumina-reinforced Sn-Sb-Cu-based composite coating from the cross section taken by SEM. Image analysis demonstrates a coating thickness of $361 \pm 16\ \mu\text{m}$. The SEM imaging shows a dense microstructure with a low porosity. As verified by x-ray microcomputed tomography, the coating exhibits an overall porosity of 1.31 vol.% (measured with a voxel edge length of 70 nm). The cross-sectional analysis reveals that the coating consists of a metallic matrix (bright phase) with different polyhedral-shaped phases distributed in the metallic matrix and scattered randomly across the coating. As obtained from the BSE imaging, the polyhedral-shaped phases contain different chemical compositions. Figure 4 shows the coating microstructure in a magnified view taken from an etched cross section (i.e., chemical etching with a 4% solution of nitric acid in ethanol) as well as the corresponding EDS maps obtained from O K α , Al K α , Cu K α , Sn L α and Sb L α . The EDS counts suggest that the matrix comprises a Sn-Sb-rich phase, which make up the largest share of the coating. Individual spots of the Sn-Sb-rich matrix differ in their elemental concentrations (i.e., Sn and Sb concentrations). Moreover, the EDS maps show the presence of alumina and Cu-rich particles both embedded in the Sn-Sb-rich matrix. The formation of further oxides can largely be excluded by EDS. With regard to the alumina particles, the image analysis reveals a mean alumina content of $5.4 \pm 1.0\ \text{area}\ \%$, which is distinctly reduced compared to the nominal composition of the starting power mixture. A possible explanation could be a poor wetting behavior between the alumina particles and the metallic matrices during spraying, as well as the resulting rebound effect of

Fig. 4 EDS maps showing the element concentrations at the coating cross section (chemically etched with a 4% solution of nitric acid in ethanol)



the non-molten alumina particles at the moment of impact onto the substrate or sublayers. EDS line scans across alumina particles, Cu-rich particles, as well as conspicuous Sn-Sb-rich particles were conducted to analyze the distribution of elements. Figure 5 shows the EDS line scan on an alumina particle (e.g., enlarged section, dark gray phase). As demonstrated by the EDS counts, the Al and O concentrations indicate alumina and preclude the presence of distinct metallurgical interactions with the surrounding matrix. With regard to Sn-Sb-rich particles (e.g., enlarged section, bright phase), the EDS line scan suggests a mixture of Sn and Sb with an almost equal atomic ratio, leading to the assumption being an intermetallic phase. For the less abundant Cu-rich particles (e.g., enlarged section, spattered/irregular shaped gray phase), besides Cu a small proportion of Sn can be detected.

The XRD analysis (Fig. 6) reveals that the coating mainly consists of Sn, SbSn (rock-salt structure) and Cu. Moreover, the XRD pattern shows the absence of intermetallic compounds such as Cu_3Sn and monoclinic Cu_6Sn_5 within the experimental resolution. However, weak Bragg

reflections of hexagonal CuSn were observed. The inset of Fig. 6 shows parts of the two-dimensional diffraction patterns of the feedstock (left) and the coating (right). While on the left side, a Debye–Scherrer ring of Sb (102) reflection is visible besides speckles caused by relatively large Sn crystals ((020), (011), (220) and (121) reflections), on the right side the Sb reflection is replaced by the reflection of SbSn ((200) and (202) reflection). The spackle pattern of Sn has changed to homogenous rings with a slight texture. Based on the findings, it can be assumed that large fractions of Sn crystals were melted during the coating process and recrystallized on the substrate yielding nearly an ideal, powder-like crystallite distribution. This effect is not observed in the case of SbSn formation. Here, still an inhomogeneous intensity distribution is obtained within the Debye–Scherrer rings pointing to relatively large crystallites. Due to the weak scattering of Al and O in comparison with Cu, Sn and Sb and the high crystallinity of the alumina, which cause only the appearance of a few spots on the two-dimensional detector, the alumina Bragg reflections are strongly suppressed in Fig. 6.

Fig. 5 EDS line scans at different regions of interest, i.e., along embedded alumina, Sn- and Cu-rich particles to the surrounding Sn-Sb-rich matrix (chemically etched with a 4% solution of nitric acid in ethanol)

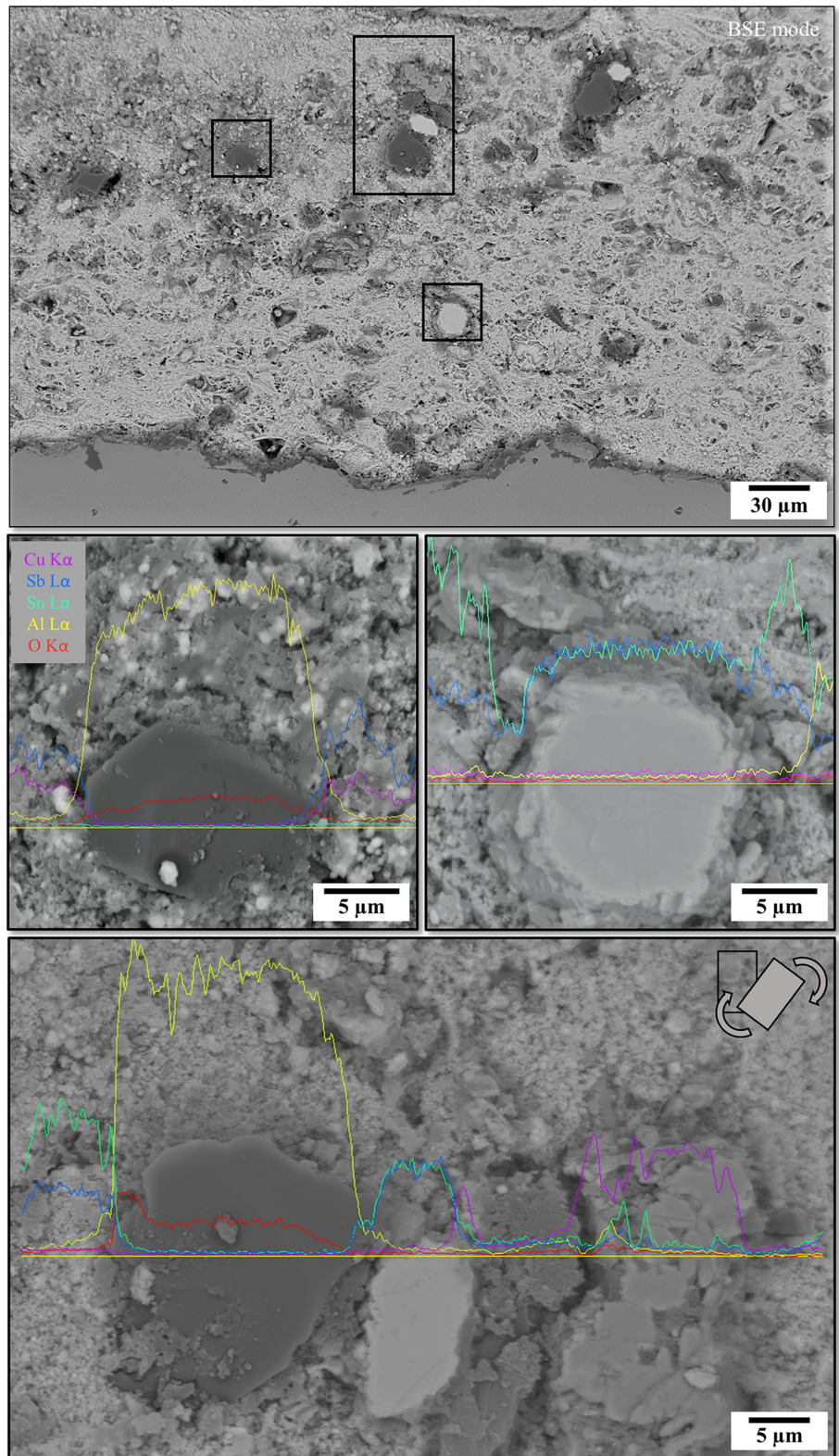
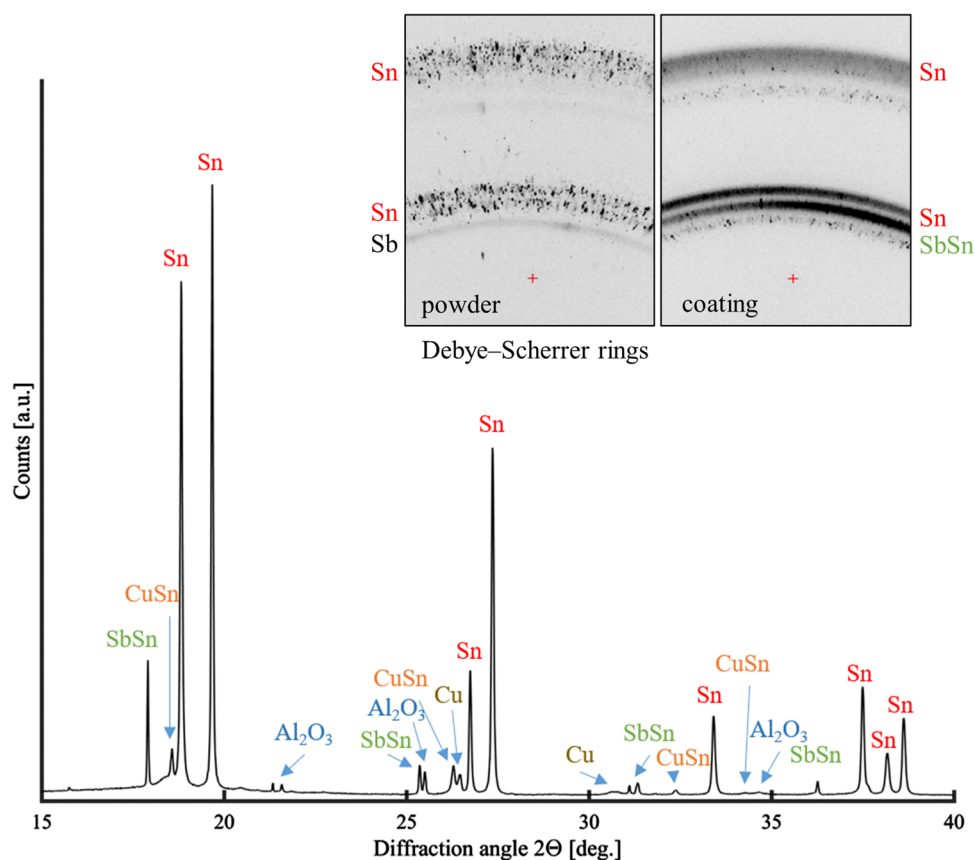


Fig. 6 XRD patterns of the alumina-reinforced Sn-Sb-Cu-based composite coating and starting powder mixture (feedstock)



Tribological Properties

The ground and polished alumina-reinforced Sn-Sb-Cu-based composite coating has a coating thickness of $224 \pm 12 \mu\text{m}$ (i.e., the standard deviation is due to the interface roughness). The dry sliding experiments reveal that the coating exhibits a wear coefficient k of $17.27 \pm 7.77 \cdot 10^{-5} \text{ mm}^3 \text{ Nm}^{-1}$, whereas the 100Cr6 counterbody demonstrates a wear coefficient k_{ball} of $0.87 \pm 0.27 \times 10^{-5} \text{ mm}^3 \text{ N m}^{-1}$. Regarding the mechanical response, Vickers microhardness measurement reveals a microhardness of $18.9 \pm 1.4 \text{ HV0.3}$ inside the wear track, whereas the non-tribological stressed surface exhibits a microhardness of $15.1 \pm 3.0 \text{ HV0.3}$. The measurements indicate an increase in microhardness of about 20% at the wear track. Nevertheless, the microhardness is distinctly lower when compared to those obtained from Babbitt coatings deposited by arc spraying ($26.9 \pm 3.7 \text{ HV0.05}$), flame spraying ($22.2 \pm 1.6 \text{ HV0.05}$), centrifugal casting ($31.2 \pm 0.8 \text{ HV0.05}$) or conventional casting ($25.2 \pm 2.8 \text{ HV0.05}$) (Ref 20). It is stated that the absence of Cu_3Sn and Cu_6Sn_5 , as repeatedly found for common Babbitt alloys, constitutes the reduction in microhardness. Instead, the formation of SbSn intermetallic phases dispersed in the soft Sn-Sb-rich matrix

predominantly affects the resulting microhardness of the low-pressure cold-sprayed alumina-reinforced Sn-Sb-Cu-based composite coating.

Figure 7 shows the worn surface of the tribological stressed alumina-reinforced Sn-Sb-Cu-based composite coating which has been sliding against the 100Cr6 counterbody. The BSE imaging suggests the presence of a tribo-oxidatively formed thin layer which covers a large amount of the sliding surface. EDS maps obtained from O K α , Fe K α , Cu K α , Al K α , Sn K α and Sb K α confirm a small amount of Fe as well as a higher concentration of O inside the wear track, suggesting that the tribo-oxidatively formed layer can be assigned to Fe-rich oxides. However, XRD data taken from the wear track do not show additional Bragg reflections of Fe-rich oxides or other oxides (e.g., tin oxides) within the experimental resolution.

The worn surface morphologies after sliding against the 100Cr6 counterbody were further analyzed by means of SEM (Fig. 8) in order to investigate the wear mechanisms more extensively. The SE imaging (Fig. 8 top) reveals the occurrence of grooves and furrows which run through the surface in the direction of sliding. Analyzing the geometry and orientation of grooves and furrows suggests that they are formed as the consequence of abrasion due to wear particles and/or by the discontinuous plowing of asperities

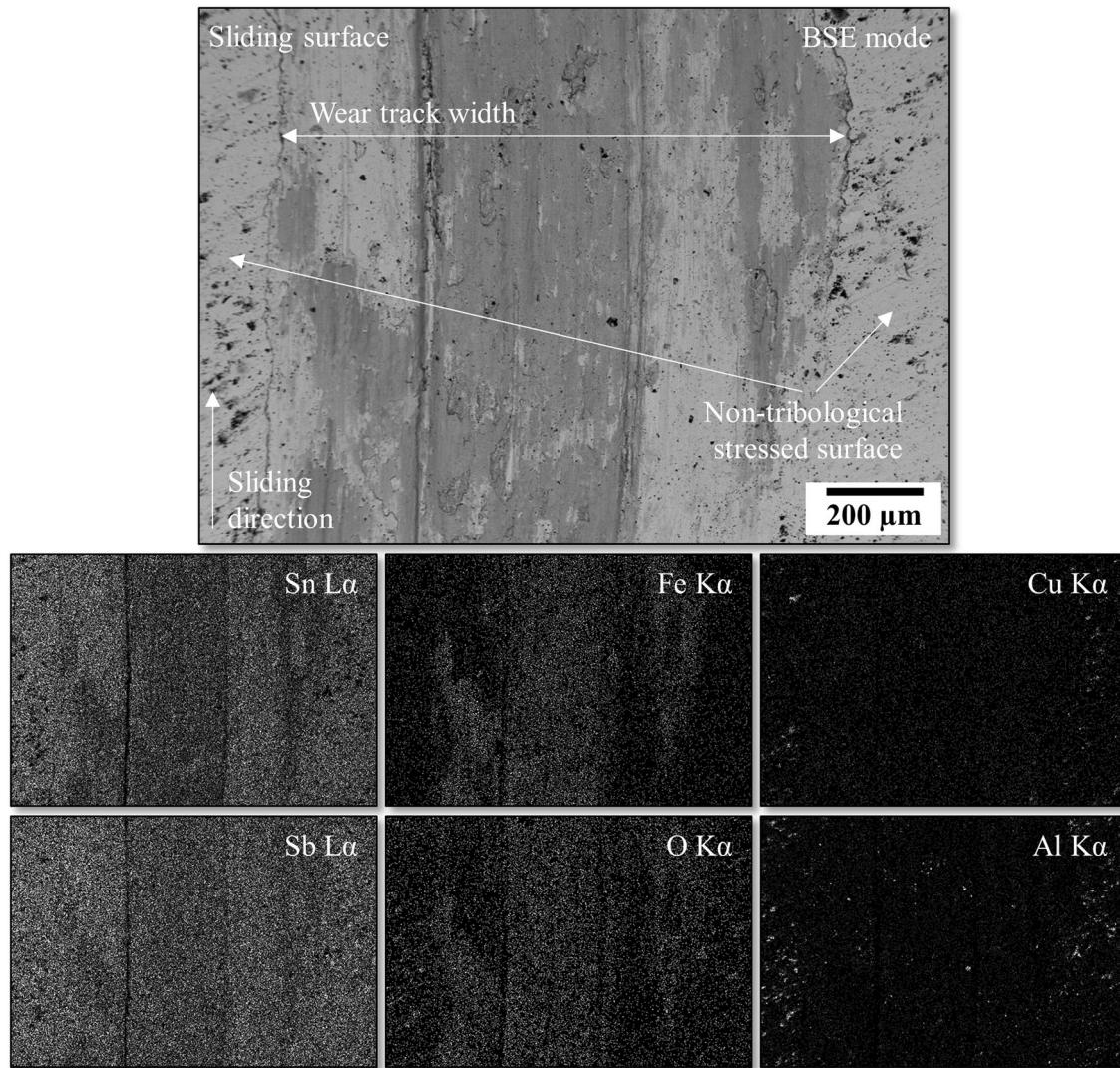


Fig. 7 SEM image and EDS maps obtained from O K α , Fe K α , Cu K α , Al K α , Sn L α and Sb L α at the tribological stressed alumina reinforced Sn-Sb-Cu-based composite coating surface after sliding against the 100Cr6 counterbody

originating from the counterbody. Hardly any surface deformations such as shear tongues or smearing can be recognized. Instead, the SE imaging clearly shows the appearance of surface spallation or pitting, indicating the surface fatigue. The process of surface spalling can be visualized for different regions of interest (Fig. 8 middle). Fracture morphologies at the spalled area (Fig. 8 middle, e.g., spot A) suggest that fatigue cracks are subsurface-initiated. Crack formation at the surface or next to regions of surface spallation occurs as a consequence of stress cracking beneath the surface. In this context, it is assumed that due to the cycling movement of the 100Cr6 counterbody (i.e., ball) over the coating surface, the coating surface is subjected to Hertzian contact stress. The material suffers from the mechanical cycling loads, which results in crack initiation. With recurrent overruns, the cracks

continue to propagate and favor surface spallation. It is striking, however, that this phenomenon has been repeatedly observed, although it can be assumed that the metallic matrix would behave ductile. A possible explanation could be the fact that cracking occurs predominantly in areas where sharp alumina particles are embedded beneath the surface.

Figure 9 shows the wear flat on the 100Cr6 counterbody after sliding against the alumina-reinforced Sn-Sb-Cu-based composite coating. EDS maps obtained from Fe K α , Cr K α , Sn L α and Sb L α demonstrate the concentrations of elements at the wear flat. The SE imaging reveals the presence of a distinct material removal accompanied by grooves and furrows, indicating that the counterbody is worn abrasively. The BSE imaging points out the existence of some material accumulations being drawn out in the

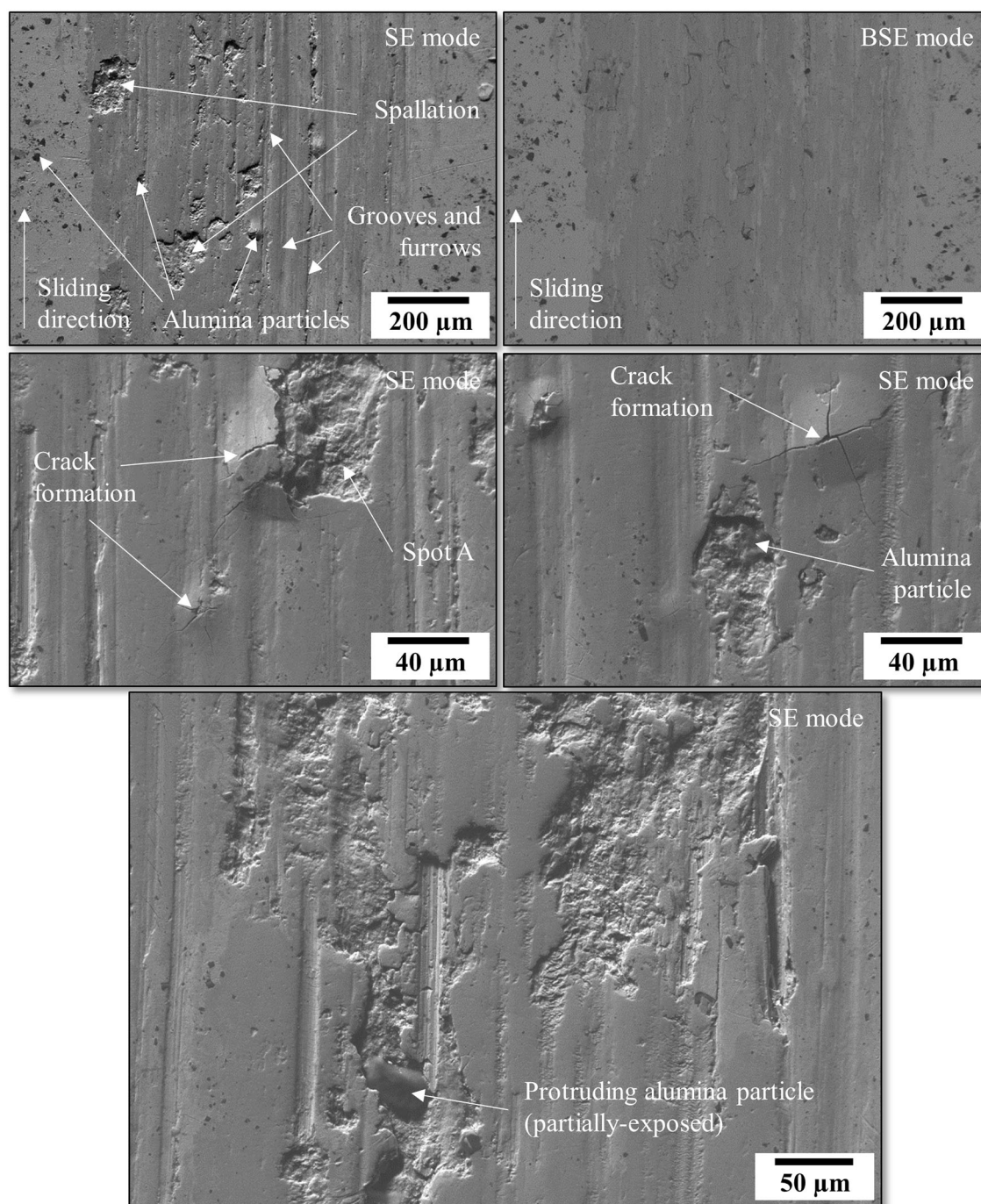


Fig. 8 SEM images showing different surface morphologies at the worn coating surface

direction of sliding. EDS analyses confirm that the material consists of Sn and Sb, suggesting additional adhesive wear for the 100Cr6 counterbody.

The findings of the local worn surfaces (i.e., the tribological stressed alumina-reinforced Sn-Sb-Cu-based composite coating and the 100Cr6 counterbody) reveal the following: (1) A small amount of Fe, originating from the 100Cr6 counterbody, is transferred to the coating; (2) a

tribo-oxidatively formed layer is observed at the coating; (3) a small amount of Sn and Sb adheres at the wear flat of the 100Cr6 counterbody; (4) despite slight adhesive wear, the 100Cr6 counterbody shows abrasion as dominant wear mechanism, whereas surface fatigue and abrasion are predominantly observed for the coating. The findings substantiate the assumption that the low shear strength phase in the alumina-reinforced Sn-Sb-Cu-based composite

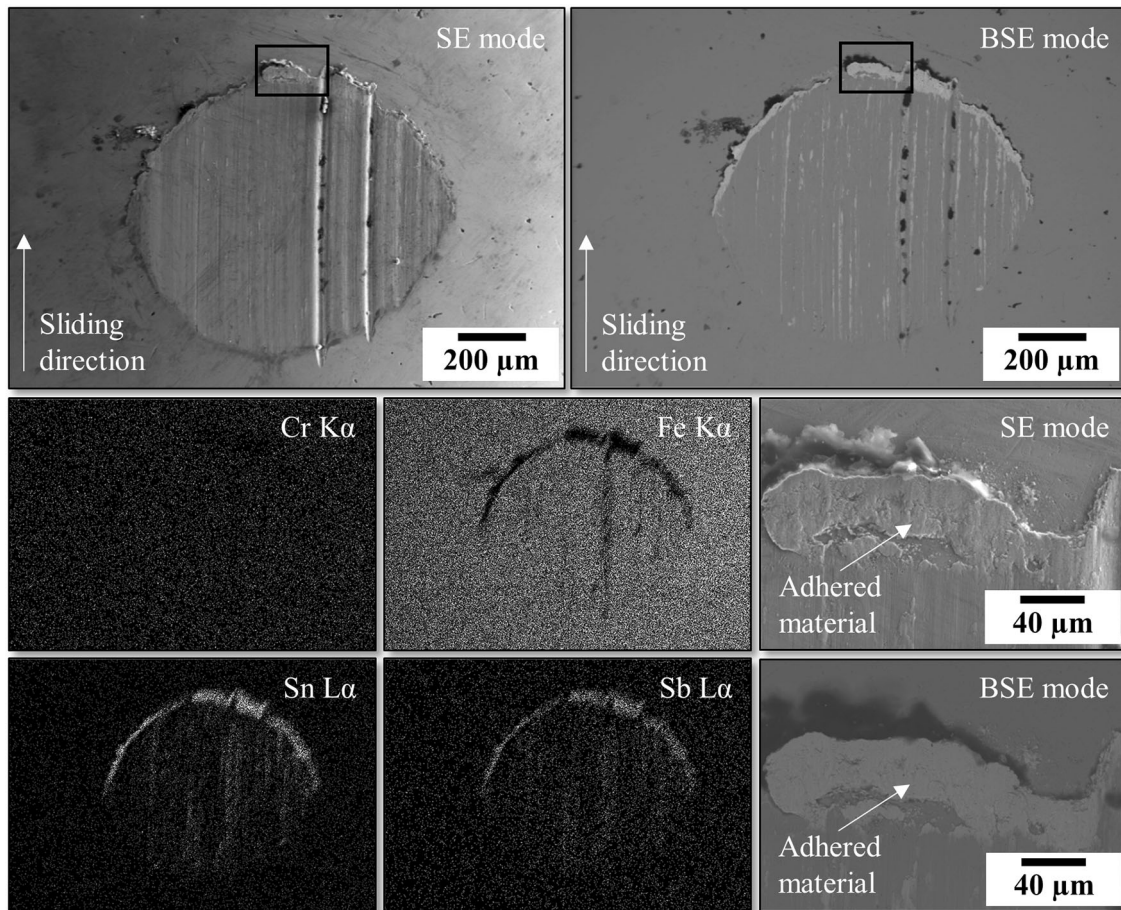


Fig. 9 SEM images and EDS maps obtained from Cr K α , Fe K α , Sn L α and Sb L α at the wear flat on the 100Cr6 counterbody after sliding against the alumina-reinforced Sn-Sb-Cu-based composite coating

coating tends to be torn out, which is subsequently transferred to the 100Cr6 counterbody. During sliding, the adherent material at the wear flat of the 100Cr6 counterbody smeared out and spread over the contact area in the direction of sliding. It follows that the protruding alumina particles in the coating (e.g., Fig. 8 bottom) or torn out alumina particles (i.e., particle breakouts) get in between the two sliding surfaces, thus removing the adherent material at the wear flat of the 100Cr6 counterbody. Simultaneously, the alumina particles tend to tumble or plow through the softer Sn-Sb-Cu-based composite coating as well as the 100Cr6 counterbody, which in turn causes abrasion. In this respect, the observations suggest that the wear mode for abrasion is most likely a combination of two-body and three-body wear.

With regard to the friction behavior, the COF indicates a running-in behavior in the beginning of the tribological test which has stabilized approximately after 100 m, and remains nearly constant with increasing sliding distance (Fig. 10). As a result, the alumina-reinforced Sn-Sb-Cu-based composite coating exhibits a mean COF of

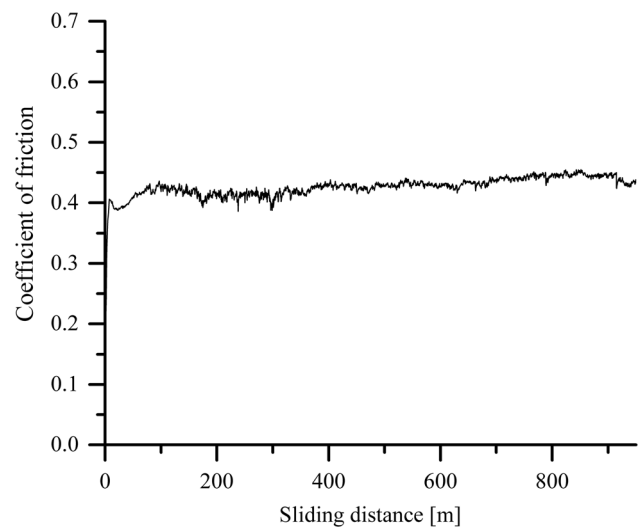


Fig. 10 Evolution of COF with increasing sliding distance

0.43 ± 0.01 sliding against the 100Cr6 counterbody. No reference values for the friction behavior of thermally sprayed ceramic-reinforced Babbitt composite coatings can

be found in the literature. Nevertheless, for weld overlays (i.e., a Babbitt composite coating reinforced with micron-sized ceramic particles), Kalashnikov et al. (Ref 12) evaluated a COF of approximately 0.4 sliding against steel. When compared to common Babbitt coatings, the findings within this study indicate that the COF of the alumina-reinforced Sn-Sb-Cu-based composite coating produced by LPCS is found to be higher than the COF of Babbitt coatings (i.e., ASTM B23 grade 2) deposited by conventional casting, but slightly lower than the COF as reported for arc and flame sprayed Babbitt coatings (Ref 20). Analyzing the data, it is striking that the COF remains stable with growing sliding distance running against 100Cr6. It is assumed that the constantly recurring adherent material (i.e., at the 100Cr6 counterbody) in the contact zone between the two sliding surfaces is removed by the alumina particles being torn out from the alumina-reinforced Sn-Sb-Cu-based composite coating, thus plowing through the contact zone. The authors (Ref 12) also ascertained a constant COF throughout the load interval for a ceramic particle-reinforced Babbitt composite coating. Simultaneously, the authors determined increased fluctuations in the COF for a common Babbitt coating which served as reference. However, a detailed analysis of the COF depending on the sliding distance was not taken into consideration. Some controversial assertions on the matter of the sliding distance and its effect on the COF are found in the literature. For several grades of Babbitt alloys, Leszczyńska-Madej et al. (Ref 32) clarified that usually the COF in dry sliding experiments continuously increases with progressing sliding distance. As reported by the authors, the increase in the COF is accompanied by significant fluctuations which were attributed to distinct adhesive wear which was also assigned as dominating wear mechanism during sliding. In contrast, Zhang et al. (Ref 33) and Junior et al. (Ref 20) reported a stable COF for Babbitt alloy, and thermally sprayed Babbitt coatings, respectively. Looking more closely at the results, it is stated that a reduced sliding distance was considered in this study, which allows a comparison only to a limited extent.

Conclusion

In this study, a first attempt was made to manufacture an alumina-reinforced Sn-Sb-Cu-based composite coating on flat samples by means of LPCS using a modified nozzle configuration which enables the coating of internal diameters of cylindrical components. Metallographic investigations of cross sections verify a dense microstructure without significant macroscopic defects, demonstrating the feasibility of depositing alumina-reinforced Sn-Sb-Cu-based composite coatings by means of LPCS. Electron

microscopy and EDS indicate that the produced composite coating exhibits a heterogeneous microstructure. Alumina particles are randomly distributed within a small portion in the coating and are embedded in a metallic matrix with its microstructural features (i.e., splat-like structures) containing different chemical compositions. XRD analyses show that the metallic matrix mainly consists of Sn, SbSn (rock-salt structure), Cu and hexagonal CuSn. It is found that large fractions of Sn crystals were melted during the coating process and recrystallized on the substrate. In contrast, the XRD pattern points to relatively large crystallites for SbSn. Due to the absence of Cu₃Sn and monocline Cu₆Sn₅, and despite small fraction of alumina particles, the microhardness of the Sn-Sb-Cu composite coating is predominantly determined by the formation of SbSn intermetallic phases dispersed in the soft Sn-Sb-rich matrix. Dry sliding experiments running against a 100Cr6 counterbody demonstrate a similar wear resistance and COF for the alumina-reinforced Sn-Sb-Cu-based composite coating compared to conventional Babbitt coatings. However, the wear mechanism and friction behavior differ in comparison with the wear behavior of conventional Babbitt steel pairings. There is evidence of surface spalling and pitting, indicating the surface fatigue. The low shear strength phase in the alumina-reinforced Sn-Sb-Cu-based composite coating is torn out and transferred to the wear flat on the 100Cr6 counterbody. During sliding, the protruding alumina particles in the coating or torn out alumina particles get in between the two sliding surfaces, removing the adherent material on the wear flat of the 100Cr6 counterbody. Simultaneously, the alumina particles are plowing through the sliding surfaces. Thus, despite the appearance of adhesion and tribochemical reactions as active wear mechanisms, the dominating wear mechanisms are surface fatigue as well as abrasion. The shearing-off of the adherent material and the occurrence of wear particles (i.e., primarily alumina particles) in the contact zone between the two sliding surfaces prevent an increase in the COF. As a result, the alumina-reinforced Sn-Sb-Cu-based composite coating demonstrates an almost constant COF throughout the load interval.

Acknowledgments The authors gratefully acknowledge the DELTA machine group for providing the synchrotron radiation.

Open Access This article is licensed under a Creative Commons Attribution 4.0 International License, which permits use, sharing, adaptation, distribution and reproduction in any medium or format, as long as you give appropriate credit to the original author(s) and the source, provide a link to the Creative Commons license, and indicate if changes were made. The images or other third party material in this article are included in the article's Creative Commons license, unless indicated otherwise in a credit line to the material. If material is not included in the article's Creative Commons license and your intended use is not permitted by statutory regulation or exceeds the permitted

use, you will need to obtain permission directly from the copyright holder. To view a copy of this license, visit <http://creativecommons.org/licenses/by/4.0/>.

References

1. M. Kamal, A. El-Bediwi, A.R. Lashin, and A.H. El-Zarka, Room-Temperature Indentation Creep and the Mechanical Properties of Rapidly Solidified Sn-Sb-Pb-Cu Alloys, *J. Mater. Eng. Perform.*, 2016, **25**(5), p 2084-2090
2. M. Kamal, A. Abdel-Salam, and J.C. Pieri, Modification in Tin-Antimony Alloys, *J. Mater. Sci.*, 1984, **19**(12), p 3880-3886
3. Q. Yin, G. Fan, G. Zhiyong, E.A. Stach, and Z. Guangwen, In Situ Visualization of Metallurgical Reactions in Nanoscale Cu/Sn Diffusion Couples, *Nanoscale*, 2015, **7**(11), p 4984-4994
4. G.-T. Lim, B.-J. Kim, K. Lee, J. Kim, Y.-C. Joo, and Y.-B. Park, Temperature Effect on Intermetallic Compound Growth Kinetics of Cu Pillar/Sn Bumps, *J. Electron. Mater.*, 2009, **38**(11), p 2228-2233
5. C.-Y. Yu and J.-G. Duh, Stabilization of Hexagonal Cu₆(Sn, Zn)₅ by Minor Zn Doping of Sn-Based Solder Joints, *Scripta Mater.*, 2011, **65**(9), p 783-786
6. K. Nogita, Stabilisation of Cu₆sn₅ by Ni in Sn-0.7Cu-0.05Ni Lead-Free Solder Alloys, *Intermetallics*, 2010, **18**(1), p 145-149
7. K. Nogita and T. Nishimura, Nickel-Stabilized Hexagonal (Cu, Ni)₆Sn₅ in Sn-Cu-Ni Lead-Free Solder Alloys, *Scripta Mater.*, 2008, **59**(2), p 191-194
8. S. Lidin and S.-Y. Piao, The Structure of Cu₆sn₅-Xsbx—Large Effects of Subtle Doping, *Zeitschrift für anorganische und allgemeine Chemie*, 2009, **635**(4-5), p 611-613
9. Y. Tasgin, The Effects of Boron Minerals on the Microstructure and Abrasion Resistance of Babbitt Metal (Sn-Sb-Cu) Used As Coating Materials in Hydroelectric Power Plants, *Inter. Metalcast.*, 2019, **9**(3), p 41
10. E. Feyzullahoğlu, A. Zeren, and M. Zeren, Tribological Behaviour of Tin-Based Materials and Brass in Oil Lubricated Conditions, *Mater. Des.*, 2008, **29**(3), p 714-720
11. A.R. Lashin, M. Mossa, A. El-Bediwi, and M. Kamal, Study of Some Physical Properties of the Rapidly Solidified Sn-Sb-Cu-Zn Alloys, *Mater. Des.*, 2013, **43**, p 322-326
12. I.E. Kalashnikov, A.G. Kolmakov, L.K. Bolotova, P.A. Bykov, L.I. Kobleleva, R.S. Mikheev, and M.L. Kheifets, Technological Parameters of Production and Properties of Babbit-Based Composite Surfacing Rods and Deposited Antifriction Coatings, *Inorg. Mater. Appl. Res.*, 2019, **10**(3), p 635-641
13. ASTM B23-00 (2014) Standard Specification for White Metal Bearing Alloys (Known Commercially as “Babbitt Metal”), ASTM International, West Conshohocken, PA, 2014. <http://www.astm.org/cgi-bin/resolver.cgi?B23>. Accessed April 23, 2020
14. Y. Tasgin, Effect of MgO, Al₂O₃ and FeCr₂O₄ on Microstructure and Wear Resistance of Babbitt Metal (Sn-Sb-Cu), *Mater. Res. Express*, 2019, **6**(4), p 46548
15. Q. Dong, Z. Yin, H. Li, X. Zhang, D. Jiang, and N. Zhong, Effects of Ag Micro-Addition on Structure and Mechanical Properties of Sn-11Sb-6Cu Babbitt, *Mater. Sci. Eng., A*, 2018, **722**, p 225-230
16. L. Branagan, Survey of Damage Investigation of Babbitted Industrial Bearings, *Lubricants*, 2015, **3**(2), p 91-112
17. A.R.C. Nascimento, F.B. Etouil, C. Moreau, S. Savoie, and R. Schulz, Production of Babbitt Coatings by High Velocity Oxygen Fuel (HVOF) Spraying, *J. Therm. Spray Technol.*, 2017, **26**(7), p 1732-1740
18. M.R. Dorfman, Chapter 22 - Thermal Spray Coatings, *Handbook of Environmental Degradation of Materials*, 3rd ed., M. Kutz, Ed., William Andrew Pub, Norwirth, 2018, p 469-488
19. M. J. Azizpour, S. N. H. M. Majd, Babbitt Casting and Babbitt Spraying Processes.
20. P.R.C.A. Junior and A.G.M. Pukasiewicz, Evaluation of Microstructure, Mechanical and Tribological Properties of a Babbitt Alloy Deposited by Arc and Flame Spray Processes, *Tribol. Int.*, 2019, **131**, p 148-157
21. Y.S. Korobov, S.V. Nevezhin, M.A. Filippov, V.V. Ilyushin, B.A. Potekhin, and L.V. Gogolev, Effect of Production Methods on Tribological Characteristics of Babbitt Coatings, *J. Frict. Wear*, 2012, **33**(3), p 190-194
22. N.P. Barykin, F.A. Sadykov, and I.R. Aslanian, Wear and Failure of Babbit Bushes in Steam Turbine Sliding Bearings, *J. Mater. Eng. Perform.*, 2000, **9**(1), p 110-115
23. G. A. Lamberton, K. Bl. Morey, and A. B. Witney, 2013, Cold Spray Coating Process: Patent (US9109291B2). <https://patentimages.storage.googleapis.com/bb/47/7a/436839fd00fdd2/US9109291.pdf>. Accessed April 23, 2020
24. R.G. Maev and V. Leshchynsky, 2018, Low-Pressure Cold Spray (Lpcs), Springer, Cham. https://link.springer.com/content/pdf/10.1007%2F978-3-319-67183-3_4.pdf. Accessed November 26, 2019.
25. H. Koivuluoto, A. Coleman, K. Murray, M. Kearns, and P. Vuoristo, High Pressure Cold Sprayed (HPCS) and Low Pressure Cold Sprayed (LPCS) Coatings Prepared from OFHC Cu Feedstock: Overview from Powder Characteristics to Coating Properties, *J. Therm. Spray Technol.*, 2012, **21**(5), p 1065-1075
26. M. Winnicki, M. Rutkowska-Gorczyca, A. Małachowska, T. Piwowarczyk, and A. Ambroziak, Microstructure and Corrosion Resistance of Aluminium and Copper Composite Coatings Deposited by LPCS Method, *Arch. Metall. Mater.*, 2016, **61**(4), p 1945-1952
27. H. Koivuluoto and P. Vuoristo, Effect of Powder Type and Composition on Structure and Mechanical Properties of Cu + Al₂O₃ Coatings Prepared by Using Low-Pressure Cold Spray Process, *J. Therm. Spray Technol.*, 2010, **19**(5), p 1081-1092
28. H. Koivuluoto, J. Lagerbom, M. Kylmälahti, and P. Vuoristo, Microstructure and Mechanical Properties of Low-Pressure Cold-Sprayed (LPCS) Coatings, *J. Therm. Spray Technol.*, 2008, **17**(5-6), p 721-727
29. A. Shkodkin, A. Kashirin, and O. Klyuev et al., Eds., The Basic Principles of Dymet Technology. In Building on 100 Years of Success, ASM Internat, Materials Park, 2006.
30. C.A. Widener, M.J. Carter, O.C. Ozdemir, R.H. Hrabe, B. Hoiand, T.E. Stamey, V.K. Champagne, and T.J. Eden, Application of High-Pressure Cold Spray for an Internal Bore Repair of a Navy Valve Actuator, *J. Therm. Spray Technol.*, 2016, **25**(1-2), p 193-201
31. W.-Y. Li and C.-J. Li, Optimal Design of a Novel Cold Spray Gun Nozzle at a Limited Space, *J. Therm. Spray Technol.*, 2005, **14**(3), p 391-396
32. B. Leszczyńska-Madej, M. Madej, and J. Hrabia-Wiśnios, Effect of Chemical Composition on the Microstructure and Tribological Properties of Sn-Based Alloys, *J. Mater. Eng. Perform.*, 2019, **28**(7), p 4065-4073
33. D. Zhang, J.K.L. Ho, G. Dong, H. Zhang, and M. Hua, Tribological Properties of Tin-Based Babbitt Bearing Alloy with Polyurethane Coating Under Dry and Starved Lubrication Conditions, *Tribol. Int.*, 2015, **90**, p 22-31

Publisher's Note Springer Nature remains neutral with regard to jurisdictional claims in published maps and institutional affiliations.